metals

MDPI

Article

Hot Strip Mill Processing Simulations on a Ti-Mo Microalloyed Steel Using Hot Torsion Testing

Caleb A. Felker *, John. G. Speer, Emmanuel De Moor and Kip O. Findley

Department of Metallurgical and Materials Engineering, Colorado School of Mines, Golden, CO 80401, USA; jspeer@mines.edu (J.G.S.); edemoor@mines.edu (E.D.M.); kfindley@mines.edu (K.O.F.)
* Correspondence: cafelker@mines.edu

Received: 8 January 2020; Accepted: 28 February 2020; Published: 3 March 2020

Abstract: Precipitation strengthened, fully ferritic microstructures in low-carbon, microalloyed steels are used in applications requiring enhanced stretch-flange formability. This work assesses the influence of thermomechanical processing on the evolution of austenite and the associated final ferritic microstructures. Hot strip mill processing simulations were performed on a low-carbon, titanium-molybdenum microalloyed steel using hot torsion testing to investigate the effects of extensive differences in austenite strain accumulation on austenite morphology and microstructural development after isothermal transformation. The gradient of imposed shear strain with respect to radial position inherent to torsion testing was utilized to explore the influence of strain on microstructural development for a given simulation, and a tangential cross-section technique was employed to quantify the amount of shear strain that accumulated within the austenite during testing. Greater austenite shear strain accumulation resulted in greater refinement of both the prior austenite and polygonal ferrite grain sizes. Further, polygonal ferrite grain diameter distributions were narrowed, and the presence of hard, secondary phase constituents was minimized, with greater amounts of austenite strain accumulation. The results indicate that extensive austenite strain accumulation before decomposition is required to achieve desirable, ferritic microstructures.

Keywords: low-carbon steel; microalloyed; hot torsion testing; prior austenite; polygonal ferrite

---

1. Introduction

A challenge exists in the automotive industry to develop new, hot-rolled, high-strength low-alloy (HSLA) steels offering a balance of high tensile strength and superior stretch-flange formability to reduce vehicle weight without compromising safety, performance, or manufacturability [1,2]. The steel industry has responded by developing ferritic steels strengthened with extensive nano-sized precipitation [2–4]. The single-phase ferritic matrix eliminates hard constituents and imparts superior stretch-flange formability, while its high yield and tensile strengths are derived from nano-sized precipitates. Titanium (Ti)-, niobium (Nb)-, or vanadium (V)-based microalloy systems are typically used for such HSLA steels, and molybdenum (Mo) is often added to strongly retard the precipitate coarsening rate [4,5]. Substitutional manganese (Mn) additions are also made to such HSLA steels to compensate for the low carbon levels and lower the Ar_3 transformation temperature for better refinement of the microalloy precipitation sizes [6]. However, the Mo and Mn additions can enhance the hardenability of the steel, resulting in slower austenite decomposition kinetics and hard secondary phase constituents (e.g., bainite and/or martensite) in the final microstructures. Hard constituents are undesirable because stretch-flange formability is markedly reduced due to the nucleation of voids at the interfaces between the relatively hard and soft phases [7,8]. Therefore, the ability to obtain both fine microalloy precipitates and a single-phase ferritic matrix in the final microstructure requires attention to thermomechanical processing, due to its effect on the austenite decomposition behavior [9].

Hot strip mills (HSM) are a key part of HSLA steel production. A typical, semi-continuous HSM consists of the following units: reheat furnace, roughing stand, transfer table, coilbox, finishing mill, runout table, and coiler [10]. The reheat furnace heats the slab to a suitable temperature to start hot rolling. The roughing stand is used for major reductions in slab thickness. The transfer table carries the slab, now called the transfer bar, from the roughing stand to the finishing mill. A coilbox is sometimes used to wrap the transfer bar into a coil to obtain a more uniform temperature profile [10]. The transfer bar is then delivered to the finishing mill, which is used for more precise gauge reductions. The strip is water-cooled from coolant headers along the runout table to control the final microstructure and then wrapped into a coil, which slowly cools to room temperature. Important processing steps during HSM processing to develop the desired, ferritic microstructures are controlled rolling in the finishing mill and accelerated cooling on the runout table (lowers the coiling temperature) [9].

Three types of austenite recrystallization behaviors are typical in HSM processing: static recrystallization, austenite pancaking (i.e., avoidance of recrystallization), and dynamic/metadynamic recrystallization [11]. The long interpass times and high temperatures, above the non-recrystallization temperature (T_{nr}), during rough rolling allow for nearly complete static recrystallization (SRX) to take place between rolling passes. Fine, equiaxed austenite grains are produced with negligible strain accumulation through SRX. Finish rolling is typically close to or below the T_{nr}, thus encouraging rapid strain-induced precipitation (SIP) of microalloy carbonitrides (e.g., Nb [12], Ti [13], and V [14] containing HSLA steels). These precipitates retard or even prevent the SRX of austenite grains; leading to pancaking, greater strain accumulation, and the generation of defects like dislocations and deformation bands. One of the major differences between HSM and plate mill rolling schedules is the interpass times, which are much shorter in the HSM and range from 0.2–5 s [11,15,16]. These short interpass times encourage strain accumulation and dynamic recrystallization (DRX) [11,17]. Fine, equiaxed austenite grains with negligible strain accumulation are also produced through DRX [18].

Hot torsion testing has been employed in numerous hot rolling simulations and recrystallization studies of HSLA steels for its ability to impose large amounts of strain while accurately controlling temperature, interpass time, and strain rate [9,15,18–21]. The conditioning of austenite into pancaked grains during HSM processing is important for final microstructural development. Whitley et al. [19] considered the evolution of the austenite grain morphology during hot torsion testing (shear deformation), and Figure 1 [19] shows a schematic overview of the expected austenite morphology at several stages throughout testing. The torsional axis is vertical to the page in Figure 1. Grains undergo one or both of the following processes at a given time: (i) shear deformation, thus becoming more elongated in morphology; and (ii) recrystallization, thus becoming refined and equiaxed in nature. Austenite grains are assumed to be initially equiaxed after soaking at high temperatures (Figure 1a), and they become elongated and rotated by the application of shear strain (Figure 1b) when viewed normal to the torsional axis of a cylindrical specimen [19]. If deformation occurs above the T_{nr}, SRX of the austenite is expected given sufficient interpass time (Figure 1c). However, if deformation occurs below the T_{nr}, pancaking of the austenite is expected and results in rotated grains with higher aspect ratios (Figure 1d). Austenite grains accommodate strain in this manner until there is sufficient driving force for recrystallization in the form of stored strain energy [19]. Strain-free grains can form in the regions of highest stored strain energy (e.g., grain boundaries and deformation substructure) (Figure 1e).

A metallographic technique was developed by Whitley et al. [19] to quantify the shear strain accumulation within (prior) austenite microstructures produced via hot torsion testing. Tested samples are sectioned parallel to the torsional axis and metallographically prepared to observe the prior austenitic microstructures. In this "tangential" plane cross-section, the inclination angles (θ') of prior austenite grains and other microstructural features can be measured with respect to the torsional axis and used to estimate the amount of shear strain that accumulated during testing (γ_{acc}) with the relationship

$$\gamma_{acc} = \tan(\theta'). \tag{1}$$

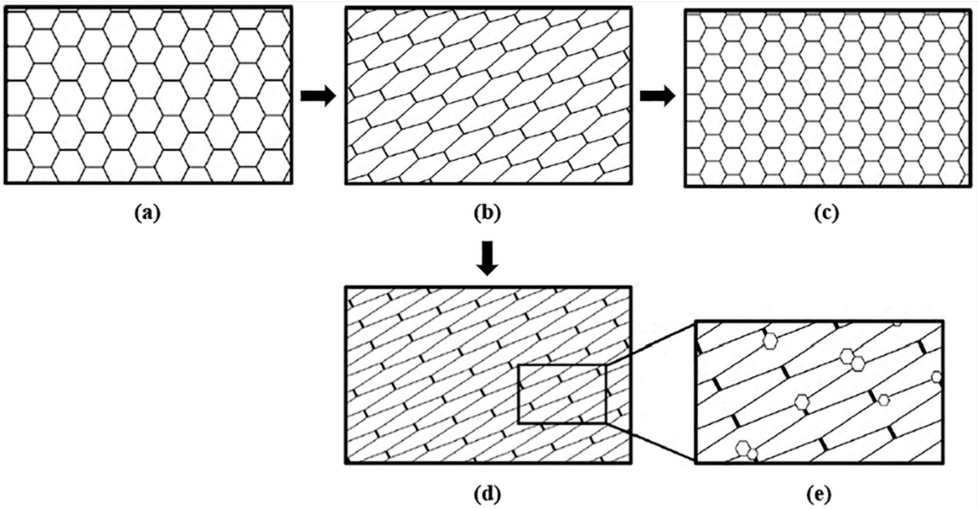

Figure 1. Schematic representation of the expected morphological evolution of austenite grains during hot torsion testing (shear deformation). The arrows indicate the progression of morphological changes. Austenite grains are (**a**) initially equiaxed and (**b**) elongate from imposed shear strain. Next, austenite grains either (**c**) recrystallize or (**d**) continue to deform in shear until (**e**) sufficient driving force is present for partial recrystallization. The torsional axis is vertical to the page. Adapted with permission from [19].

Multiple austenite deformation-recrystallization cycles during multi-pass torsion testing can result in mixed (prior) austenite microstructures displaying a distribution of inclination angles [18]. These distributions reflect the local variation in strain accumulation that can result during thermomechanical processing. Figure 2 [19] shows an example of this technique applied to a 1045 steel microalloyed with V that underwent industrial bar rolling simulations via hot torsion testing. Various microstructural features are highlighted with their corresponding inclination angles with respect to the torsional axis, which indicated:

(A) Manganese sulfide (MnS) inclusion, elongated and initially oriented parallel to the rolling direction. Since MnS inclusions do not recrystallize during thermomechanical processing, γ_{acc} represents the total shear strain imposed;

(B) Highly elongated prior austenite grain with the same inclination angle as MnS, suggesting no recrystallization during thermomechanical processing;

(C) Elongated prior austenite grain with an inclination angle less than (A) and (B), indicating some degree of recrystallization during thermomechanical processing, followed by subsequent deformation. The measured inclination angle represents the amount of shear strain that accumulated after the last recrystallization event, assuming an equiaxed grain morphology after recrystallization;

(D) Fine, equiaxed prior austenite grains that indicate recrystallization without shear strain accumulation.

The main aim of this work was to investigate differences in austenite strain accumulation before decomposition and the associated influence on (prior) austenite morphology and microstructural development after isothermal transformation for a low-carbon, Ti-Mo microalloyed steel.

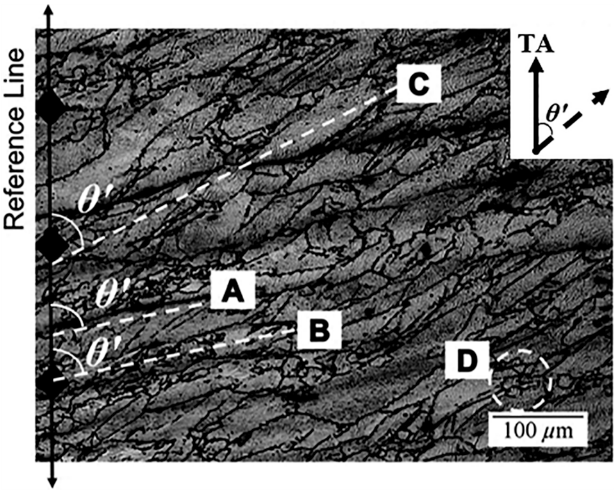

Figure 2. Light optical micrograph from the tangential plane cross-section of the prior austenite microstructure produced via industrial bar rolling simulations on a 1045 steel microalloyed with V using hot torsion testing. MnS inclusions (A) and some austenite grains (B) accumulate all imposed shear strain without recrystallizing. Other austenite grains (C) deform in shear after recrystallizing or (D) recrystallize following the final deformation pass. The torsional axis (TA) is vertical to the page, parallel to the reference line indicated. Adapted with permission from [19].

2. Materials and Methods

A low-carbon, Ti-Mo microalloyed steel was investigated, and its chemical composition is shown in Table 1. The experimental alloy was received as 16 mm thick, hot-rolled steel from Baoshan Iron & Steel Co. (Shanghai, China). Table 2 provides estimates of particular critical transformation temperatures using empirical equations found in the literature. These critical transformation temperatures were used to guide the thermomechanical processing of the experimental alloy. The following empirical equations were used: Andrews for Ac_1 and Ac_3 [22], Schacht for Ar_1 [23], Pickering for Ar_3 [24], Lee #2 for B_s [25], and Borrato for T_{nr} [26]. The M_s temperature was determined experimentally using dilatometry [27].

Table 1. Experimental Alloy Composition.

Wt pct	C	Mn	Si	Mo	Ti	Al	N	S	P	Fe
Ti-Mo	0.053	1.86	0.10	0.24	0.120	0.035	0.0036	0.0024	0.0085	Balance

Table 2. Critical Transformation Temperature Estimates for the Experimental Alloy.

°C	Ac_1	Ac_3	Ar_1	Ar_3	B_s	M_s	T_{nr}
Ti-Mo	706	875	725	871	606	362	995
Reference	[22]	[22]	[23]	[24]	[25]	Experimental	[26]

Solutionizing temperatures for relevant compounds in austenite were determined based on solubility expressions [28,29]. The calculations showed that titanium nitride (TiN) remains undissolved during solid-state processing, thus all nitrogen (N) was assumed to be removed from solid solution. The evolution of equilibrium phases as a function of temperature was predicted with Thermo-Calc® (Thermo-Calc Software, Solna, Sweden, Version 2019) using the TCFE9 database (assuming all N was already incorporated into TiN precipitates), and the results are shown in Figure 3. The MC equilibrium phase represents a mixed microalloy carbide exhibiting the NaCl (B1) crystal structure without the incorporation of N. From the determined equilibrium dissolution temperature of MC, a soaking temperature of 1250 °C was selected.

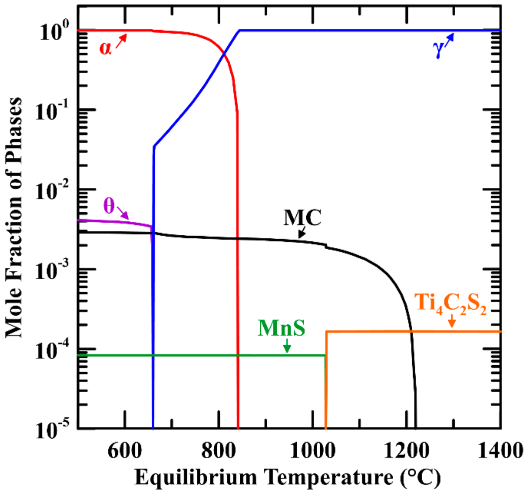

Figure 3. Evolution of equilibrium phases as a function of temperature predicted with Thermo-Calc® using the TCFE9 database. It was assumed that all N was first incorporated into TiN precipitates at much higher temperatures (greater than 1500 °C).

2.1. Hot Torsion Testing

Hot torsion testing was accomplished using a Gleeble® 3500 system equipped with the Hot Torsion Mobile Conversion Unit (Dynamic Systems Inc., Poestenkill, NY, USA). Sub-sized torsion samples were machined from the as-received material according to the schematic illustration in Figure 4, where the rolling direction was parallel to their lengths. Figure 5 shows a photograph inside the Hot Torsion Mobile Conversion Unit chamber, highlighting the setup used during testing. Both ends of the sample were restrained to keep the reduced gauge length fixed during torsion testing, and the Gleeble® 3500 was programmed to minimize axial stresses by adjusting the stroke arm. Axial stresses did not exceed ±10 Mpa during testing. Helium (He) gas was used as the quenchant for all tests and was directed from quench heads both in front and behind the sample. The torsion motor coupler within the Hot Torsion Mobile Conversion Unit was set for 20° free rotation, which allowed rapid acceleration of the torsion motor during deformation as well as a rapid reduction in torque on the sample during interpass times. Hot torsion testing was performed under the protective environment of argon (Ar) gas to minimize oxidation and decarburization near the surface of the sample. The oxygen partial pressure within the chamber was maintained under 30 ppm during testing and monitored using a PurgEye® 200 oxygen sensor (Huntingdon Fusion Techniques, Burry Port, UK).

The temperature of each sample was monitored at the mid-length of the reduced gauge section using a Metis Model MQ11 optical pyrometer (Process Sensors Corporation, Milford, MA, USA) that was calibrated at 1100 °C prior to testing. The pyrometer is not reliable below ~700 °C, so it was used to control temperature during heating, soaking, and deformation. An alternative method was required to control temperature during the accelerated cooling and isothermal holding steps due to the relatively low temperatures employed. Attaching a thermocouple to the fixed shoulder of the sample, where limited deformation occurs, and accounting for the temperature difference between the shoulder and mid-length of the reduced gauge section, proved to be an efficient method for controlling temperatures below ~700 °C. Therefore, a Type K thermocouple was spot welded to the surface of the sample roughly 0.5 mm away from the fixed shoulder (as shown in Figure 5) for testing that included isothermal holding. Each thermocouple wire was insulated with a small section of ceramic tubing to prevent short-circuiting. An isothermal holding temperature of 650 °C was planned, and preliminary testing showed that an offset value of approximately 18 °C (i.e., shoulder temperature of 632 °C) was appropriate to account for the temperature difference between the shoulder and reduced gauge section.

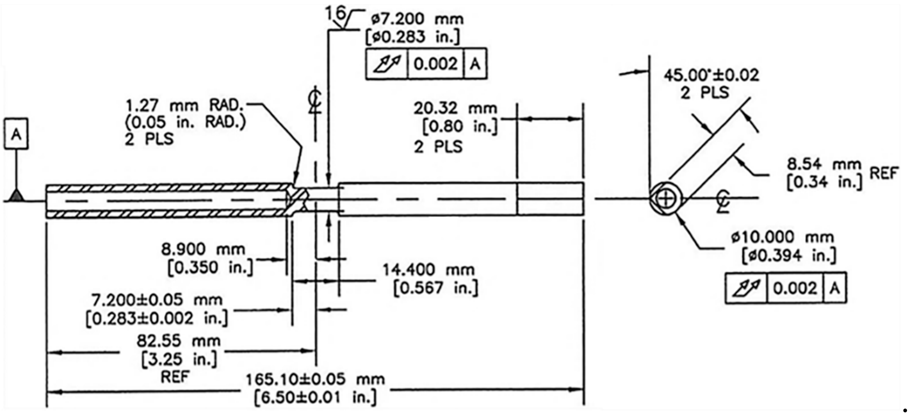

Figure 4. Schematic illustration of the sub-sized torsion samples tested with the Gleeble® 3500. Note the reduced gauge section and hollow ends. The hollow ends allow for a fairly consistent cross-sectional area throughout the entire sample and improve temperature uniformity during testing.

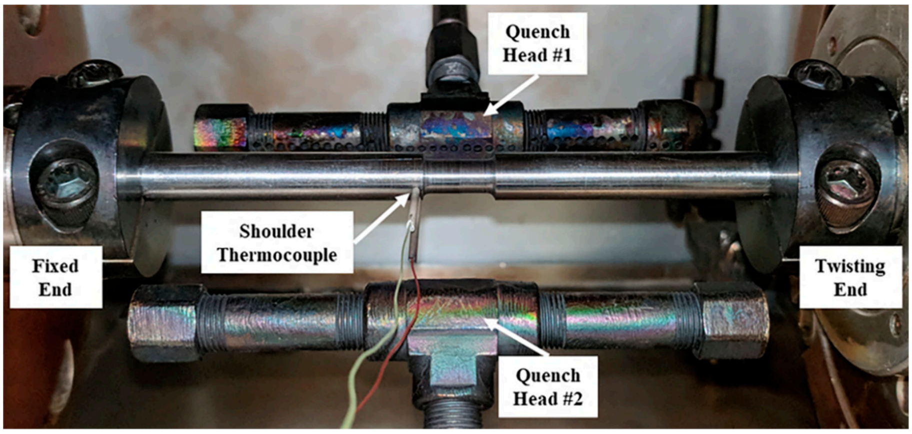

Figure 5. Photograph inside the Gleeble® 3500 Hot Torsion Mobile Conversion Unit chamber highlighting the hot torsion setup. The shoulder thermocouple was required to control temperature during accelerated cooling and isothermal holding.

Microstructural gradients within samples undergoing torsion testing require the selection of a specific radial position to determine deformation parameters since imposed shear strain (γ) varies with the radius of the reduced gauge section (r), according to

$$\gamma = \frac{r\,\varphi}{L} = \tan(\theta), \tag{2}$$

where φ is the angle of twist (in radians), L is the reduced gauge length of the sample, and θ is the expected inclination angle with respect to the torsional axis corresponding to the imposed shear strain. The radial position used in this work to determine deformation parameters during HSM processing simulations was the "effective radius", which is positioned at 72.4 pct of the radial distance from the central axis [30]. Barraclough et al. showed that this location represents the bulk behavior for materials having a wide variety of strain rate sensitivities and/or strain hardening behaviors [30].

The following equations were used to convert the pass-by-pass shear strains and strain rates into appropriate angles of twist and twisting times for simulation purposes, as well as to convert the resulting torque to shear stress. The angle of twist for each pass was calculated according to

$$\varphi = \frac{\gamma\,L}{0.724r}, \tag{3}$$

and the twisting time (t) for each pass was calculated according to

$$t = \frac{\gamma}{\dot{\gamma}}, \tag{4}$$

where $\dot{\gamma}$ is the shear strain rate. Barraclough et al. [30] developed an equation to convert torque (Γ) to shear stress (τ) considering the effective radius, which assumes pure torsion and uniform shear strain along the length of the reduced gauge section

$$\tau = \frac{3\Gamma}{2\pi[(r_2)^3 - (r_1)^3]}, \tag{5}$$

where r_2 is the outer surface radius and r_1 is the inner surface radius. Finally, the shear stress and strain values were converted to equivalent true stress (σ) and strain (ε) values by applying the Von Mises criterion

$$\sigma = \sqrt{3}\tau, \tag{6}$$

$$\varepsilon = \frac{\gamma}{\sqrt{3}}, \tag{7}$$

and used to determine the MFS for each pass according to

$$\text{MFS} = \frac{1}{\varepsilon_b - \varepsilon_a} \int_{\varepsilon_a}^{\varepsilon_b} \sigma \, d\varepsilon, \tag{8}$$

where ε_a and ε_b are the initial and final equivalent true strains per pass, respectively. The integrals were solved using analytical solutions of logarithmic regressions of the data according to

$$\int_{\varepsilon_a}^{\varepsilon_b} (a_1 \ln(\varepsilon) + b_1) d\varepsilon = [(a_1 \varepsilon) \ln(\varepsilon) - a_1 \varepsilon + b_1 \varepsilon] \,\Big|_{\varepsilon_a}^{\varepsilon_b}, \tag{9}$$

where a_1 and b_1 are constants. This approach typically assumes uniform constitutive mechanical properties of the material through the cross-section.

Table 3 summarizes the hot torsion testing schedule applied. The testing parameters were developed after consideration of the literature [9,11,15,18] and industrial processing [16,31]. Samples were heated at 5 °C/s to a soaking temperature of 1250 °C and held for 5 min to dissolve microalloy carbides. Rough rolling simulations consisted of four identical passes between 1240 and 1150 °C, each with relatively long interpass times to promote SRX of the austenite. Finish rolling simulations consisted of seven passes: either between 1150 and 1000 °C (designated as High T Finish) or between 1050 and 900 °C (designated as Low T Finish). Note that the designations of either High T Finish or Low T Finish simulations include the identical rough rolling simulations. These temperature ranges were selected to be above or mostly below the estimated T_{nr} of approximately 1000 °C to develop (prior) austenite microstructures with drastically different strain accumulation prior to decomposition. The roughing-to-finishing delay was 30 and 100 s for the High T Finish and Low T Finish simulations, respectively. Short interpass times are typical during HSM processing, which promote austenite pancaking and possibly DRX of the austenite later during finish rolling [11,15,16]. Overall, the amounts of true strain imparted during rough and finish rolling simulations were about 1.60 and 2.40, respectively, totaling about 4.00. The cooling rate between all passes was kept constant at 5 °C/s to ensure accurate temperature control. Additionally, relatively low target shear strain rates were utilized to ensure accuracy of the imparted shear strains. After the last finishing pass (F7), samples were either: (i) quenched as rapidly as possible (~43 °C/s) to room temperature to investigate the prior austenite grain (PAG) size and morphology, or (ii) accelerated cooled at ~30 °C/s to an isothermal holding temperature of 650 °C, held for 30 min, and finally quenched as rapidly as possible to room temperature to investigate polygonal ferrite characteristics and the presence of any secondary phase constituents.

Table 3. Hot Torsion Testing Schedule to Simulate High T Finish* and Low T Finish** Processing.

Pass No.	Temperature (°C)	True Strain	Shear Strain	Twist Angle (rad)	Shear Strain Rate (s^{-1})	Interpass Time (s)
R1	1240	0.40	0.80	4.42	5	20
R2	1210	0.40	0.80	4.42	5	20
R3	1180	0.40	0.80	4.42	5	20
R4	1150	0.40	0.80	4.42	5	30* or 100**
F1	1150* or 1050**	0.50	1.00	5.52	10	8
F2	1110* or 1010**	0.50	1.00	5.52	10	8
F3	1070* or 970**	0.40	0.80	4.42	10	6
F4	1040* or 940**	0.40	0.80	4.42	10	4
F5	1020* or 920**	0.30	0.60	3.31	10	2
F6	1010* or 910**	0.20	0.40	2.21	10	2
F7	1000* or 900**	0.10	0.20	1.10	10	Quench or Hold

Previous research [19] has shown that a tangential orientation is best for investigating PAG morphologies and quantifying the amount of shear strain that accumulated within the microstructure for samples tested via hot torsion. This orientation is presented schematically in Figure 6. Tested samples were prepared in the tangential orientation according to the following procedure. First, the reduced gauge section was cut free from its ends on both sides of the sample. Next, the gauge section was cut in half (perpendicular to the torsional axis) to reveal the "thermal plane". Note that the thermal plane corresponds to the mid-length of the reduced gauge section, approximately where the optical pyrometer was aligned prior to testing. Then, each piece was cut in half (parallel to the torsional axis). Finally, these quartered sections were mounted in Bakelite and precision ground to the radial position of interest using measurements of chord length to reveal the tangential plane.

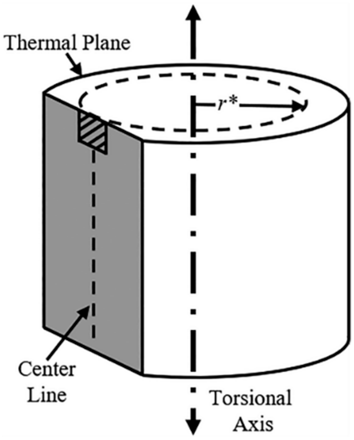

Figure 6. Schematic of the tangential orientation (evaluated at some radial position, *r**) of samples tested via hot torsion. The shaded region represents the tangential plane of interest, and the boxed region represents the approximate location of microstructural characterization.

In addition to the effective radius, two other radial positions were selected to further investigate how strain influences austenite conditioning and the final microstructures during HSM processing. Recall that shear strain varies with the radius of the reduced gauge section according to Equation (2). The target shear strain for the HSM processing simulations was 8.00, where the effective radius (0.724 radial position) was used to determine the deformation parameters. Radial positions of 0.50 and 0.90 were also selected to represent an extensive range of possible shear strain accumulation.

The approximate shear strain for the 0.50 radial position is 5.52, which might represent processing of thicker gauge material, and the approximate shear strain for the 0.90 radial position is 9.94, which might represent processing of thinner gauge material. All three radial positions were investigated using the tangential orientation for each condition produced via hot torsion testing.

2.2. Microstructural Characterization

Samples for microscopic evaluation were sectioned, mounted in Bakelite, and prepared using standard metallographic procedures. Samples were etched with either a 1 pct nital or a modified Béchet–Beaujard reagent. The 1 pct nital reagent was used to reveal ferrite grain boundaries and secondary phase constituents. The modified Béchet-Beaujard reagent was used to reveal PAG boundaries and consisted of 200 cm^3 of deionized water, 2.6 g of picric acid solids, 8 cm^3 of Teepol (wetting agent), and 2 cm^3 of hydrochloric acid. This reagent was heated to 65 °C on a temperature-controlled hot plate equipped with a thermocouple feedback and stirred with a magnetic stir rod throughout the etching process. After each interval of etching with the modified Béchet-Beaujard reagent, samples were immersed in a methanol bath, ultrasonicated, and dried with a heat gun. PAG boundaries were highlighted in black to enhance their clarity within the provided micrographs.

General imaging of microstructures was accomplished using light optical microscopy (LOM), where the micrographs were used to determine average grain size, phase area fraction, etc. LOM was performed with an Olympus Model PMG3 inverted light microscope (LECO Corporation, St. Joseph, MI, USA) with a PAXcam Model PX-CM digital camera (MIS Inc., Villa Park, IL, USA) and PAX-it! Image analysis software (MIS Inc., Villa Park, IL, USA, Version 7.8). Electron backscatter diffraction (EBSD) analysis was performed on isothermally transformed microstructures with a JSM-7000F field emission-scanning electron microscope (JEOL USA Inc., Peabody, MA, USA) to investigate polygonal ferrite grain diameter distributions. Prior to EBSD analysis, samples were metallographically prepared and vibratory polished for at least 4 h using 0.02 μm colloidal silica solution. EBSD scans were performed at an accelerating voltage of 20 keV, calibrated EBSD camera working distance of 18 mm, and step size of 0.1 μm. EBSD data were collected with a Hikari Pro detector (EDAX Inc., Mahwah, NJ, USA) using the TEAM^{TM} software (EDAX Inc., Mahwah, NJ, USA, Version 4.5), and the datasets were analyzed with the Orientation Imaging Microscopy Analysis© software (EDAX Inc., Mahwah, NJ, USA, Version 8.1). EBSD datasets were cleaned using the following functions: Neighbor Orientation Correction (Level 3, Tolerance 5.0, Minimum Confidence Index (CI) 0.10); Grain CI Standardization (Tolerance 5.0, Minimum Size 3, Multi Row 1); and Neighbor CI Correlation (Minimum CI 0.30, Single Iteration).

Polygonal ferrite and prior austenite grain sizes were determined with the concentric circle method utilizing the ImageJ software (open-source). The intercepts of the circles with the grain boundaries were counted, and the average intercept lengths were calculated and reported as the average grain sizes. A total of 1000 or more grain boundary intercepts were counted for each condition to determine a representative grain size. Note that prior austenitic twins were observed within some PAGs, but these were not considered in the PAG size measurements. Aspect ratios of the PAGs were determined by measuring the major and minor axes of individual grains (assuming an elliptical shape) with the ImageJ software and calculating their ratios. Inclination angles of the PAGs with respect to the torsional axis were measured with the ImageJ software and used to quantify the amount of shear strain that accumulated within the (prior) austenite microstructures using the previously described metallographic technique developed by Whitley et al. [19]. A total of 100 or more PAGs were measured for each condition to determine a representative aspect ratio and inclination angle.

The ImageJ software was also used to determine the area fraction of secondary-phase constituents using an image thresholding procedure. This procedure was employed because of the distinct difference in the etching response of the polygonal ferrite (carbon depleted) and secondary phase constituents (carbon rich) with 1 pct nital. First, LOM micrographs were thresholded from grayscale images to black-and-white images using a grayscale value range that best captured the secondary phase constituents but without capturing polygonal ferrite grain boundaries. After thresholding, pixels in the desired grayscale value range were transformed to white pixels (representing the secondary phase constituents), while all other pixels were transformed to black pixels (representing polygonal ferrite). Figure 7 provides an example of the thresholding process. Finally, the ratio of the number of white or black pixels to the total number of pixels was used to determine the secondary phase constituents or polygonal ferrite area fractions, respectively. This procedure was repeated at five or more different areas of the microstructure for each condition to determine representative phase area fractions.

Samples were metallographically prepared and etched with 1 pct nital prior to Vickers microhardness testing in order to relate microhardness to microstructural features. Vickers microhardness testing was performed with a LM110 hardness tester (LECO Corporation, St. Joseph, MI, USA) according to ASTM Standard E384-17 [32]. A 5 × 5 array of indents with an indentation load of 100 g was used to determine the representative values of the polygonal ferrite in each isothermally transformed condition. Indentations immediately adjacent to secondary phase constituents (including large TiN precipitates) were disregarded. Very low indentation loads of 10 g were used to investigate the small secondary phase constituents. Note that indentation loads like 10 g can result in consistently higher microhardness values [33], so values determined with this indentation load were used for comparison only.

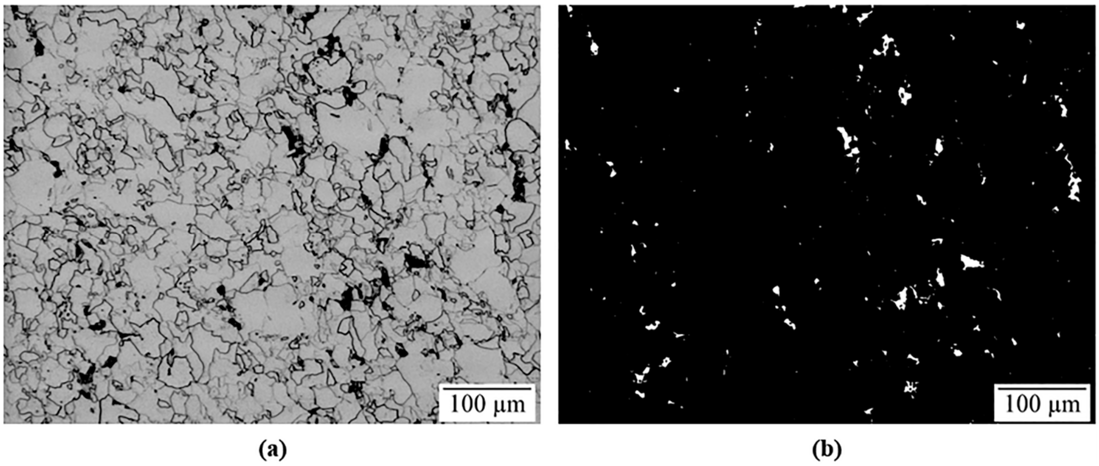

Figure 7. Example of the image thresholding process used to determine the area fraction of constituent phases in mixed microstructures: (**a**) original light optical microscopy (LOM) micrograph, where light etched regions represent polygonal ferrite and dark etched regions represent the secondary phase constituents, and (**b**) processed image, where black pixels represent polygonal ferrite and white pixels represent the secondary phase constituents.

3. Results

3.1. Strain Accumulation in the (Prior) Austenite

Figure 8 shows the MFS as a function of inverse absolute temperature for the (a) High T Finish and (b) Low T Finish HSM processing simulations. Two linear regressions are included in each figure: the first for the roughing stage and the second for the finishing stage (without including the softening regions). Note that the imparted shear strain was incrementally reduced from the F1 to F7 deformation steps (1.00 to 0.20) during finish rolling simulations, and deformation parameters were identical between High T Finish and Low T Finish simulations. The relatively low imparted shear strain for the F7 deformation step (0.20) contributed to the drop in the MFS observed for that deformation step in both simulations. Thus, the data obtained from the F7 deformation steps were not considered in the analysis. The MFS continuously increased from the F1 to F6 deformation steps for High T Finish simulations. However, a softening region was indicated following the F4 deformation step for Low T Finish simulations. This softening region was not indicated for High T Finish simulations when subjected to identical strains per pass. The rates at which MFS increased with respect to inverse absolute temperature were similar between the two rolling simulations for both the roughing and finishing stages. Low T Finish simulations were expected to cause a sharper increase in the rate at which MFS changed with respect to absolute temperature relative to High T Finish simulations, but this behavior was not observed. The lack of a sharper increase in the rate of change in MFS with respect to absolute temperature for Low T Finish simulations may be due to limited strain-induced precipitation as a result of the finish rolling start (F1) temperature being above the estimated T_{nr} coupled with the relatively short interpass times. However, the magnitudes of the MFS were greater overall for the Low T Finish simulations, since lower deformation temperatures were employed. The softening region indicated in the last passes near the end of Low T Finish simulations may suggest recrystallization of the austenite after extensive strain accumulation. Characterization of the prior austenite microstructures of samples quenched immediately after the final finishing deformation step (F7) was performed for each simulation to relate the observed PAG morphology with the amount of shear strain that accumulated during thermomechanical processing. Additionally, a separate sample underwent Low T Finish simulations but was quenched after the fourth finishing deformation step (F4) to investigate the prior austenite microstructure immediately preceding the softening region indicated in Figure 8b.

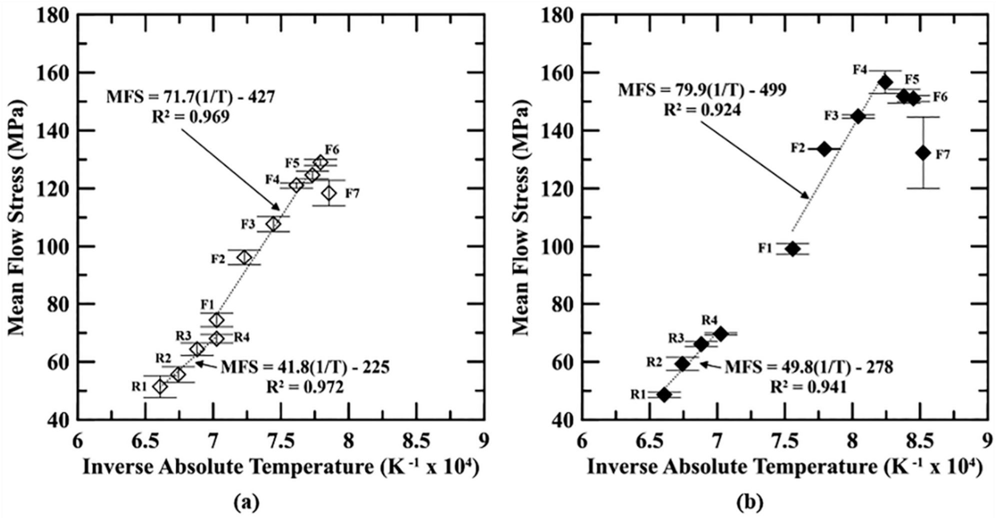

(a) (b)

Figure 8. Summary of mean flow stress as a function of inverse absolute temperature for (**a**) High T Finish and (**b**) Low T Finish simulations via hot torsion testing. Two linear regressions are included in each figure: the first for the roughing stage (R) and the second for the finishing stage (F), excluding the softening region. The error bars represent one standard deviation.

The prior austenite microstructures produced via hot torsion testing are shown in Figure 9 after etching with a modified Béchet-Beaujard reagent. Samples that underwent High T Finish simulations are shown in Figure 9a–c, and samples that underwent Low T Finish simulations are shown in Figure 9d–f. Three radial positions are shown for each HSM processing simulation: mid-radius, 0.50 (a and d); effective radius, 0.724 (b and e); and near-surface, 0.90 (c and f). PAG sizes were significantly refined for Low T Finish simulations (roughly 6–9 μm) compared to High T Finish simulations (roughly 14–15 μm). PAGs were mostly equiaxed for High T Finish simulations, and the (prior) austenite was only slightly refined by the additional strain near the surface. However, Low T Finish simulations resulted in mixed (prior) austenite microstructures consisting of larger, pancaked, and aligned grains and smaller, equiaxed grains. PAGs were not inclined to the torsional axis (horizontal to the page) for High T Finish simulations, but PAGs were inclined to the torsional axis for Low T Finish simulations and exhibited an average inclination angle of approximately 60 ± 10°. Interestingly, the average inclination angles for the Low T Finish simulations were consistent between the three radial positions investigated. This average prior austenite inclination angle corresponds to an accumulation of roughly 1.7 shear strain (0.85 true strain) within the microstructure according to Equation (1). If no shear strain accumulates during rough rolling simulations, a total of 4.8 shear strain could accumulate during finish rolling simulations. Therefore, roughly 36 pct of the total shear strain is accumulated during Low T Finish simulations, while negligible shear strain is accumulated during High T Finish simulations. The differences in prior austenite morphology are highlighted in Figure 10, where higher magnification images are shown for the 0.724 radial position.

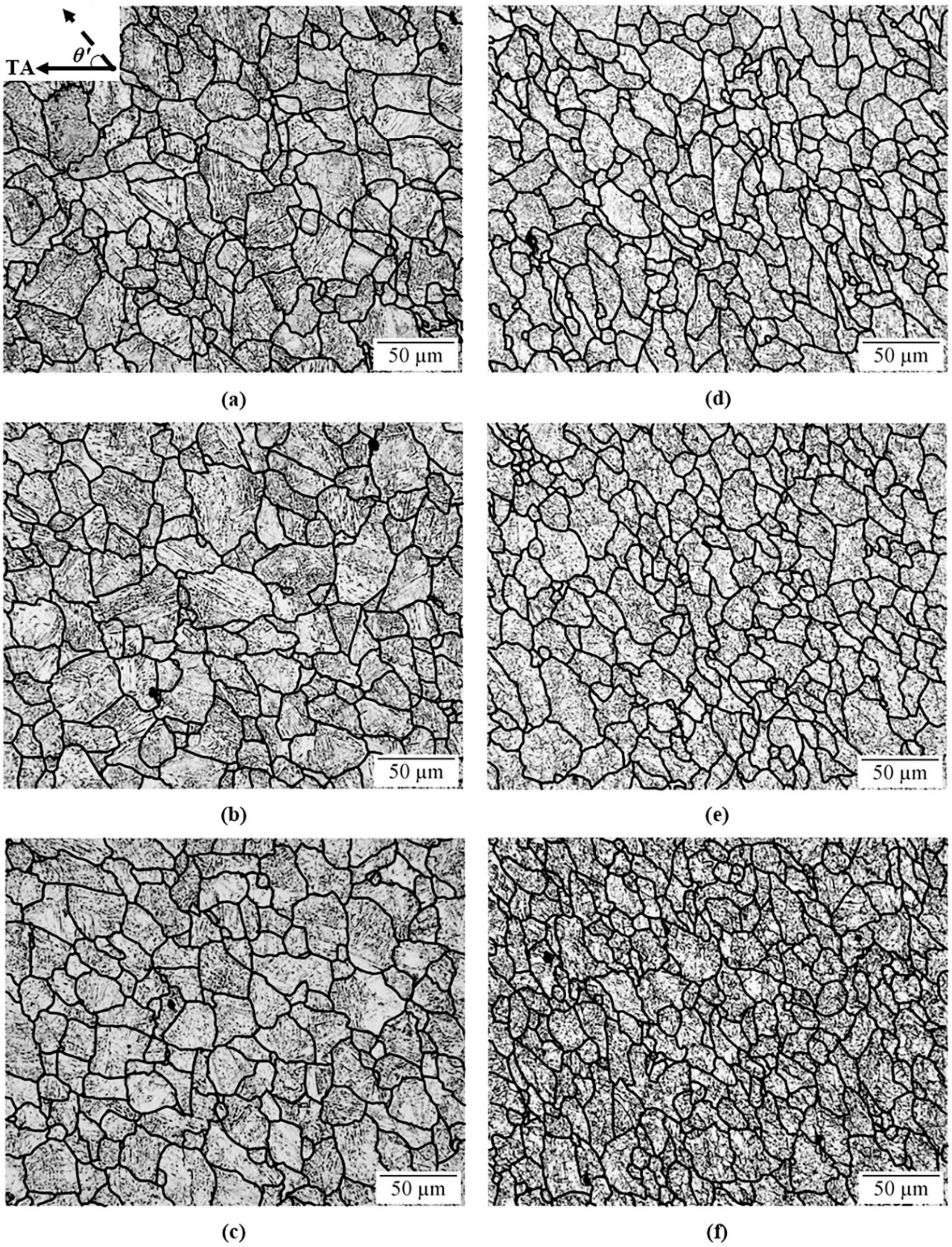

(a) (d)

(b) (e)

(c) (f)

Figure 9. LOM micrographs of the prior austenite microstructures produced via (**a**–**c**) High T Finish and (**d**–**f**) Low T Finish simulations. The following radial positions are shown: (**a**) and (**d**) 0.50; (**b**) and © 0.724; and (**c**) and (**f**) 0.90. The torsional axis (TA) is horizontal to the page. Etched with a modified Béchet-Beaujard reagent, and prior austenite grain boundaries are highlighted in black.

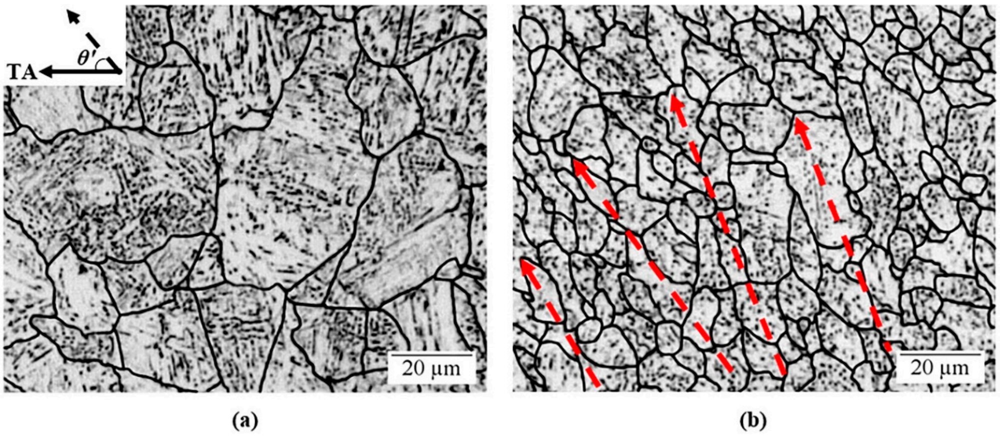

Figure 10. Higher magnification LOM micrographs of the prior austenite microstructures produced via (**a**) High T Finish and (**b**) Low T Finish simulations highlighting differences in morphology. The 0.724 radial position is shown in both. The torsional axis (TA) is horizontal to the page. Dashed lines in (**b**) show the inclination angles of various prior austenite grains. Etched with a modified Béchet-Beaujard reagent, and prior austenite grain boundaries are highlighted in black.

Figure 11 summarizes the average PAG (a) size and (b) aspect ratio with respect to radial position determined for microstructures produced via High T Finish and Low T Finish simulations. Note that as radial position increases (towards the surface), the amount of shear strain imposed during torsion testing increases according to Equation (2). PAG size decreases with increasing radial position for both High T Finish and Low T Finish simulations. Radial position had a greater influence on PAG size refinement for Low T Finish simulations compared to High T Finish simulations. PAG aspect ratios ranged between approximately 1–2 and 1–3.5 for High T Finish and Low T Finish simulations, respectively, considering all radial positions. The large range of PAG aspect ratios for Low T Finish simulations was a result of its mixed nature involving pancaked grains with higher aspect ratios along with fine, equiaxed grains with lower aspect ratios. The PAG morphology becomes more equiaxed with increasing radial position, especially for Low T Finish simulations. The micrographs provided in Figure 9d–f and data summarized in Figure 11 suggest that greater imposed shear strain results in a greater amount of fine, equiaxed (prior) austenite grains for Low T Finish simulations. The prior austenite microstructures and MFS results are consistent with the occurrence of recrystallization due to high strain accumulation.

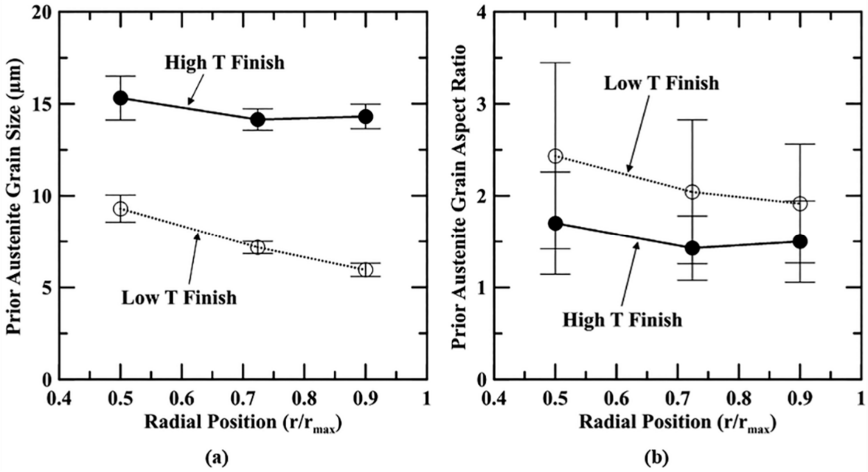

Figure 11. Prior austenite grain (**a**) size and (**b**) aspect ratio with respect to radial position determined for microstructures produced via High T Finish and Low T Finish simulations. The error bars represent one standard deviation.

The prior austenite microstructure produced via Low T Finish simulations and quenched after the fourth finishing deformation step (F4) is shown in Figure 12 after etching with a modified Béchet–Beaujard reagent. Only the 0.724 radial position is shown. PAGs were mostly pancaked and inclined to the torsional axis, but some fine, equiaxed grains can also be observed (Figure 12b). The PAG size was approximately 11 ± 1 µm, which was greater than the PAG size that resulted from quenching after the final finishing deformation step (F7). That value was approximately 7.2 ± 0.3 µm at the effective radius. The finer and more equiaxed (prior) austenitic microstructure obtained after complete Low T Finish simulations compared to quenching after the F4 step suggests that more austenite recrystallization occurred (whether statically and/or dynamically) due to the additional shear strain that was imparted during thermomechanical processing. Figure 13 shows PAG inclination angle histograms constructed for Low T Finish simulations quenched after the (a) F4 step and (b) F7 step. Data were collected at the 0.724 radial position. Interestingly, both simulations resulted in similar distributions of inclination angles, and the average inclination angles were determined to be 60° ± 8° and 59° ± 10° for interrupted and complete Low T Finish simulations, respectively. This microstructural inclination angle may correspond to a critical amount of shear strain (approximately 1.7) that must accumulate during thermomechanical processing before a significant driving force for austenite recrystallization is available.

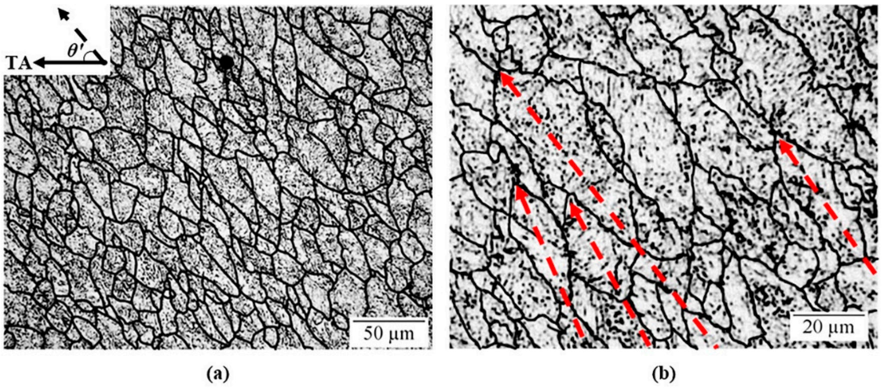

Figure 12. LOM micrographs of the prior austenite microstructures produced via Low T Finish simulations and quenched after the fourth finishing deformation step (F4): (**a**) lower and (**b**) higher magnification. The 0.724 radial position is shown in both. The torsional axis (TA) is horizontal to the page. Dashed lines in (**b**) show the inclination angles of various prior austenite grains. Etched with a modified Béchet–Beaujard reagent, and prior austenite grain boundaries are highlighted in black.

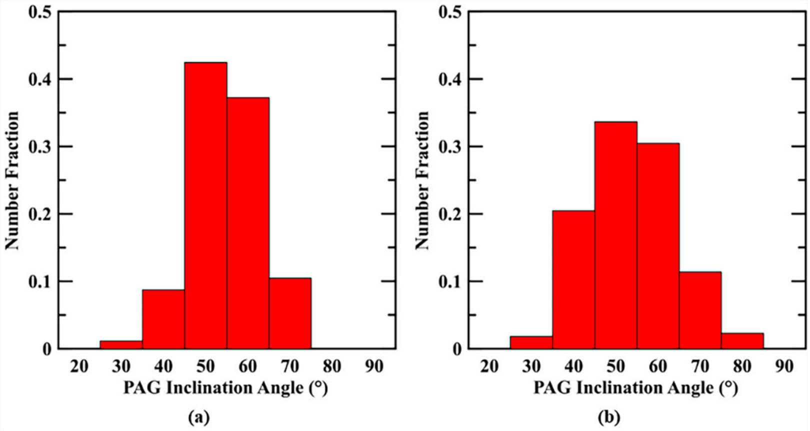

Figure 13. Prior austenite grain (PAG) inclination angle histograms for microstructures produced via Low T Finish simulations: (**a**) quenched after the fourth finishing deformation step (F4) and (**b**) quenched after the final finishing deformation step (F7). Data were obtained at the 0.724 radial position for both cases.

3.2. Isothermally Transformed Microstructures

The polygonal ferrite microstructures produced via hot torsion testing followed by isothermal holding at 650 °C for 30 min are shown in Figure 14 after a 1 pct nital etch. Samples that underwent High T Finish simulations are shown in Figure 14a–c, and samples that underwent Low T Finish simulations are shown in Figure 14d–f. Three radial positions are shown for each HSM processing simulation: mid-radius, 0.50 (a and d); effective radius, 0.724 (b and e); and near-surface, 0.90 (c and f). Table 4 summarizes the average polygonal ferrite area fraction, grain size, and Vickers microhardness for each condition. All radial positions for each HSM processing simulation exhibited a mostly ferritic microstructure (greater than 97 pct), where a small amount of secondary phase constituents was observed in some conditions. However, High T Finish simulations clearly resulted in more secondary phase constituents than Low T Finish simulations. The average Vickers microhardness for the secondary phase constituents in the High T Finish and Low T Finish simulations (both evaluated at the 0.724 radial position) was approximately 550 HV (10 g). The presence of hard, secondary phase constituents negatively impacts stretch-flange formability [7,8]. Polygonal ferrite grain sizes were significantly refined for Low T Finish simulations (roughly 2.7–3.2 µm) compared to High T Finish simulations (roughly 5.2–6.0 µm). The refinement observed for Low T Finish simulations is due to the increased boundary surface area per grain volume from the austenite pancaking and generation of defects, both of which enhance the ferrite nucleation kinetics during austenite decomposition [12]. Polygonal ferrite grain sizes were relatively consistent for all the radial positions investigated for each processing simulation. Finally, polygonal ferrite microhardness was similar for the Low T Finish conditions, due in part to the refined grain size, except for the 0.90 radial position, which exhibited a marked decrease in microhardness. Thermomechanical processing may have an important influence on microalloy precipitation within the ferrite, and this behavior is being investigated in ongoing research.

Table 4. Characteristics of Isothermally Transformed Microstructures.

Simulation Designation	Radial Position	Ferrite Area Fraction (pct)	Ferrite Grain Size (µm)	Ferrite Vickers Microhardness (100 g)
High T Finish	0.50	97.4	5.4 ± 0.3	263 ± 9
	0.724	98.7	5.2 ± 0.3	271 ± 13
	0.90	> 99	6.0 ± 0.4	256 ± 8
Low T Finish	0.50	98.8	3.2 ± 0.1	283 ± 8
	0.724	> 99	3.1 ± 0.1	284 ± 6
	0.90	> 99	2.7 ± 0.05	245 ± 11

EBSD analysis of polygonal ferrite microstructures produced via both processing simulations was performed to measure grain diameter distributions. Composite image quality (IQ) and inverse pole figure (IPF) maps for the High T Finish and Low T Finish simulations are shown in Figure 15a,b, respectively, for the 0.724 radial position. These maps provide a clear delineation of polygonal ferrite grains and highlight the substantial differences in overall morphology that resulted from the different HSM processing simulations. Figure 16 shows ferrite grain diameter histograms constructed for (a) High T Finish and (b) Low T Finish simulations, where data were collected and averaged from four 90 × 90 μm^2 regions. High T Finish simulations exhibited a bimodal distribution centered around 2–4 and 10–20 µm and Low T Finish simulations exhibited a unimodal distribution centered around 1–4 µm. Additionally, the average ferrite grain diameters determined by EBSD analysis were approximately 4.8 ± 0.1 and 2.7 ± 0.1 µm for the High T Finish and Low T Finish simulations, respectively. These values are similar to the values determined via LOM using the concentric circle method for the 0.724 radial position. Overall, these data suggest that extensive austenite strain accumulation before decomposition is required to achieve fine, homogeneous microstructures of polygonal ferrite and to avoid small amounts of hard, secondary-phase constituents.

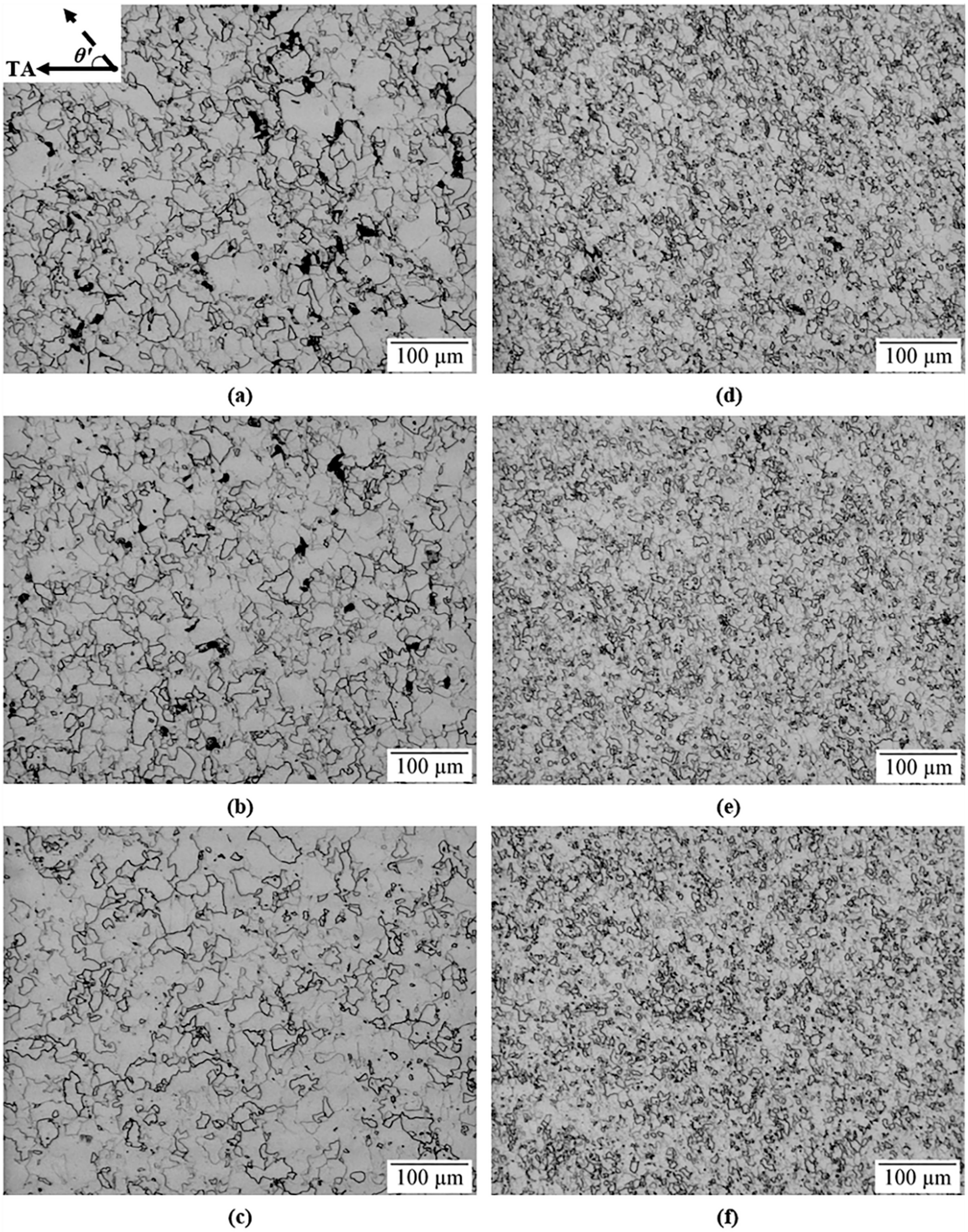

Figure 14. LOM micrographs of the polygonal ferrite microstructures produced via (**a**–**c**) High T Finish and (**d**–**f**) Low T Finish simulations followed by isothermal holding at 650 °C for 30 min. The following radial positions are shown: (**a**) and (**d**) 0.50; (**b**) and (**e**) 0.724; and (**c**) and (**f**) 0.90. The torsional axis (TA) is horizontal to the page. Etched with 1 pct nital.

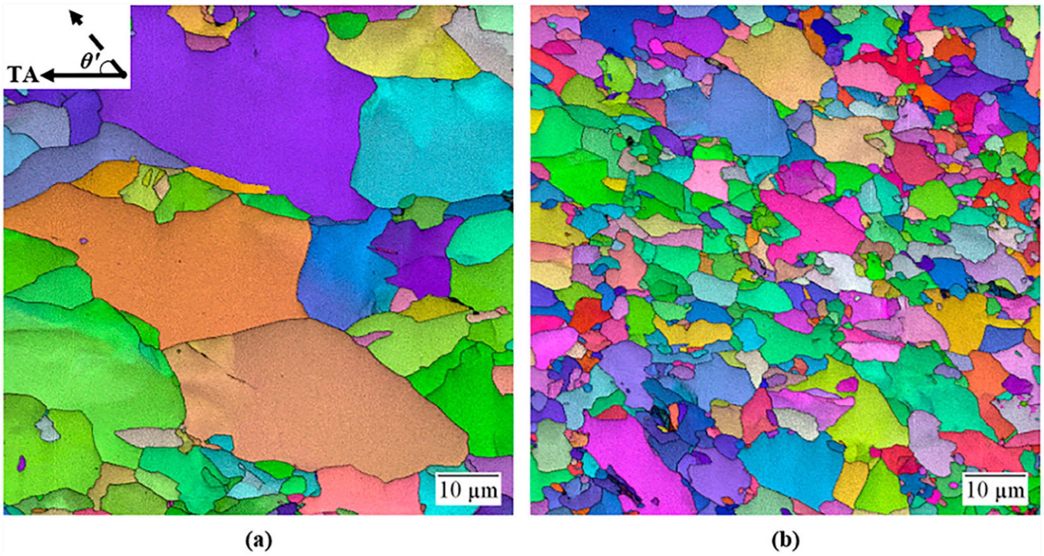

Figure 15. Composite image quality and inverse pole figure maps obtained with EBSD analysis of the polygonal ferrite microstructures produced via (**a**) High T Finish and (**b**) Low T Finish simulations followed by isothermal holding at 650 °C for 30 min. The 0.724 radial position is shown in both. The torsional axis (TA) is horizontal to the page.

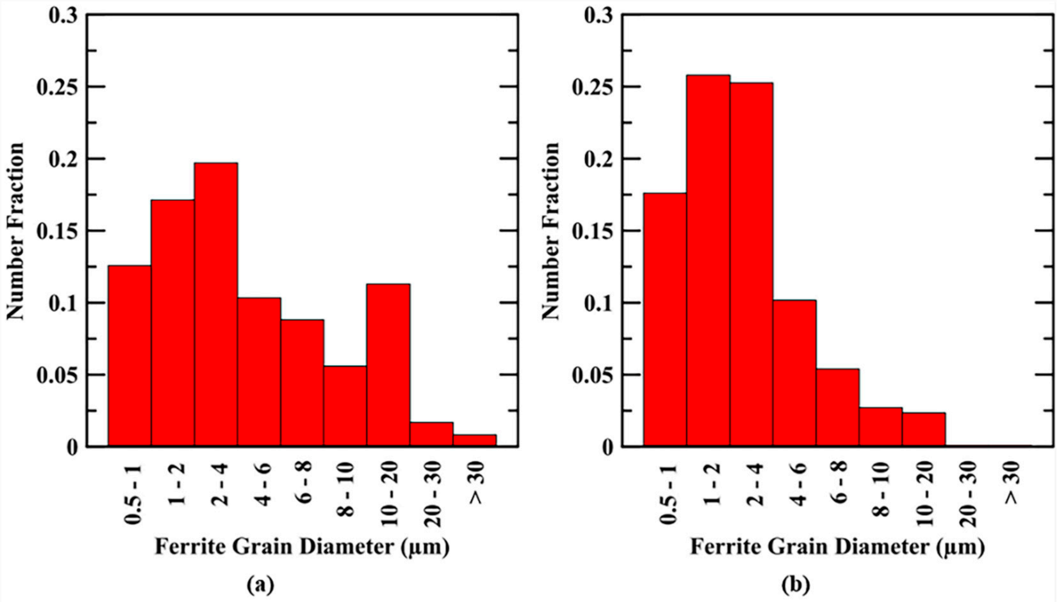

Figure 16. Ferrite grain diameter histograms obtained with EBSD analysis of the polygonal ferrite microstructures produced via (**a**) High T Finish and (**b**) Low T Finish simulations followed by isothermal holding at 650 °C for 30 min. Data were obtained at the 0.724 radial position for both.

4. Conclusions

The effects of extensive differences in austenite strain accumulation before decomposition on (prior) austenite morphology and microstructural development after isothermal transformation were investigated for a low-carbon, Ti-Mo microalloyed steel. Roughly 36 pct of the total shear strain imparted during finish rolling simulations accumulated within the prior austenitic microstructures for Low T Finish simulations, while negligible shear strain was accumulated for High T Finish simulations. The amounts of shear strain that accumulated during Low T Finish simulations were similar (roughly 1.7) at multiple radial positions subjected to different total strains, as well as for both interrupted and complete multi-pass rolling simulations. This value of accumulated shear strain may indicate a critical amount of strain that must accumulate during thermomechanical processing before a sufficient driving force for austenite recrystallization is available in this steel. Low T Finish simulations resulted in a significant refinement in PAG size compared to High T Finish simulations, and greater imposed shear strain resulted in a greater amount of fine, equiaxed austenite grains (intermixed with larger, pancaked grains) for Low T Finish simulations. Additionally, Low T Finish simulations followed by isothermal holding at 650 °C for 30 min resulted in a significant refinement in polygonal ferrite grain sizes and better homogenization compared to High T Finish simulations. Therefore, the results suggest that extensive austenite strain accumulation before decomposition is required to achieve fine, homogeneous microstructures of polygonal ferrite and to avoid small amounts of hard, secondary-phase constituents that may diminish stretch-flange formability.

Author Contributions: Conceptualization, C.A.F., J.G.S. and E.D.M.; Data curation, C.A.F.; Formal analysis, C.A.F.; Investigation, C.A.F.; Methodology, C.A.F. and J.G.S.; Project administration, J.G.S. and E.D.M.; Resources, J.G.S., E.D.M. and K.O.F.; Supervision, J.G.S. and E.D.M.; Visualization, C.A.F. and J.G.S.; Writing—original draft, C.A.F.; Writing—review and editing, J.G.S., E.D.M. and K.O.F. All authors have read and agreed to the published version of the manuscript.

Funding: This research was funded by the sponsors of the Advanced Steel Processing and Products Research Center, an NSF industry/university cooperative research center.

Acknowledgments: The authors gratefully acknowledge Huanrong Wang (Baoshan Iron & Steel Co.) for providing the experimental materials.

Conflicts of Interest: The authors declare no conflict of interest. The sponsors had no role in the execution, interpretation, or writing of the study.

References

1. Dinda, S.; DiCello, J.; Kasper, A. Using Microalloyed Steels to Reduce Weight of Automotive Parts. In Proceedings of the Microalloying 75, Washington, DC, USA, 1–3 October 1975; pp. 531–538.
2. Jha, G.; Haldar, A.; Bhaskar, M; Venugopalan, T. Development of High Strength Hot Rolled Steel Sheet for Wheel Disc Application. *Mater. Sci. Technol.* **2011**, *27*, 1131–1137. [CrossRef]
3. Kamikawa, N.; Abe, Y.; Miyamoto, G.; Funakawa, Y.; Furuhara, T. Tensile Behavior of Ti, Mo-Added Low Carbon Steels with Interphase Precipitation. *ISIJ Int.* **2014**, *54*, 212–221. [CrossRef]
4. Funakawa, Y.; Fujita, T.; Yamada, K. Metallurgical Features of NANOHITEN^{TM} and Application to Warm Stamping. *JFE Tech. Rep.* **2013**, *18*, 74–79.
5. Okamoto, R.; Borgenstam, A.; Agren, J. Interphase Precipitation in Niobium-Microalloyed Steels. *Acta Mater.* **2010**, *58*, 4783–4790. [CrossRef]
6. Funakawa, Y.; Shiozaki, T.; Tomita, K.; Yamamoto, T.; Maeda, E. Development of High Strength Hot-rolled Sheet Steel Consisting of Ferrite and Nanometer-sized Carbides. *ISIJ Int.* **2004**, *44*, 1945–1951. [CrossRef]
7. Chun, E.; Do, H.; Kim, S.; Nam, D.; Park, Y.; Kang, N. Effect of Nanocarbides and Interphase Hardness Deviation on Stretch-Flangeability in 998 MPa Hot-Rolled Steels. *Mater. Chem. Phys.* **2013**, *140*, 307–315. [CrossRef]
8. Hu, J.; Du, L.; Wang, J.; Sun, Q. Cooling Process and Mechanical Properties Design of Hot-rolled Low Carbon High Strength Microalloyed Steel for Automotive Wheel Usage. *Mater. Des.* **2014**, *53*, 332–337. [CrossRef]
9. Nakata, N.; Militzer, M. Modelling of Microstructure Evolution during Hot Rolling of a 780 MPa High Strength Steel. *ISIJ Int.* **2005**, *45*, 82–90. [CrossRef]
10. Yildiz, S.; Forbes, J.; Huang, B.; Zhang, Y.; Wang, F.; Vaculik, V.; Dudzic, M. Dynamic Modeling and Simulation of a Hot Strip Finishing Mill. *Appl. Math. Model.* **2009**, *33*, 3208–3225. [CrossRef]
11. Siciliano, F.; Jonas, J. Mathematical Modeling of the Hot Strip Rolling of Microalloyed Nb, Multiply-alloyed Cr-Mo, and Plain C-Mn Steels. *Metall. Trans. A* **2000**, *31A*, 511–530. [CrossRef]
12. Speer, J.; Hansen, S. Austenite Recrystallization and Carbonitride Precipitation in Niobium Microalloyed Steels. *Metall. Trans. A* **1989**, *20A*, 25–38. [CrossRef]
13. Wang, Z.; Zhang, H.; Guo, C.; Liu, W.; Yang, Z.; Sun, X.; Zhang, Z.; Jiang, F. Effect of Molybdenum Addition on the Precipitation of Carbides in the Austenite Matrix of Titanium Micro-alloyed Steels. *J. Mater. Sci.* **2016**, *51*, 4996–5007. [CrossRef]

14. Baker, T. Processes, Microstructure and Properties of Vanadium Microalloyed Steels. *Mater. Sci. Technol.* **2009**, *25*, 1083–1107. [CrossRef]
15. Samuel, F.; Yue, S.; Jonas, J.; Zbinden, B. Modeling of Flow Stress and Rolling Load of a Hot Strip Mill by Torsion Testing. *ISIJ Int.* **1989**, *29*, 878–886. [CrossRef]
16. Merwin, M.; U.S. Steel Research and Technology Center, Munhall, PA, USA. Personal communication, 2018.
17. Pereda, B.; Fernandez, A.; Lopez, B.; Rodriguez-Ibabe, J. Effect of Mo on Dynamic Recrystallization Behavior of Nb-Mo Microalloyed Steels. *ISIJ Int.* **2007**, *47*, 860–868. [CrossRef]
18. Samuel, F.; Yue, S.; Jonas, J.; Barnes, K. Effect of Dynamic Recrystallization on Microstructural Evolution during Strip Rolling. *ISIJ Int.* **1990**, *30*, 216–225. [CrossRef]
19. Whitley, B.; Araujo, A.; Speer, J.; Findley, K.; Matlock, D. Analysis of Microstructure in Hot Torsion Simulation. *Mater. Perform. Charact.* **2015**, *4*, 307–321. [CrossRef]
20. Bai, D.; Yue, S.; Sun, W.; Jonas, J. Effect of Deformation Parameters on the No-Recrystallization Temperature in Nb-Bearing Steels. *Metall. Trans. A* **1993**, *24A*, 2151–2159. [CrossRef]
21. Calvo, J.; Collins, L.; Yue, S. Design of Microalloyed Steel Hot Rolling Schedules by Torsion Testing: Average Schedule vs. Real Schedule. *ISIJ Int.* **2010**, *50*, 1193–1199. [CrossRef]
22. Krauss, G. Critical Temperatures. In *Steels—Processing, Structure, and Performance*, 2nd ed.; ASM International: Materials Park, OH, USA, 2015; pp. 30–32.
23. Schacht, K.; Prahl, U.; Bleck, W. Material Models and their Capability for Process and Material Properties Design in Different Forming Processes. *Mater. Sci. Forum* **2016**, *854*, 174–182. [CrossRef]
24. Pickering, F. Steels: Metallurgical Principles. In *Encyclopedia of Materials Science and Engineering*; The MIT Press: Cambridge, MA, USA, 1986.
25. Lee, Y. Empirical Formula of Isothermal Bainite Start Temperature of Steels. *J. Mater. Sci. Lett.* **2002**, *21*, 1253–1255. [CrossRef]
26. Boratto, F.; Barbosa, R.; Yue, S.; Jonas, J. Effect of Chemical Composition on the Critical Temperatures of Microalloyed Steels. Proceedings of International Conference on Physical Metallurgy of Thermomechanical Processing of Steels and Other Metals (THERMEC), Tokyo, Japan, 6–10 June 1988; pp. 383–390.
27. Yang, H.; Bhadeshia, H. Uncertainties in Dilatometric Determination of Martensite Start Temperature. *Mater. Sci. Technol.* **2007**, *23*, 556–560. [CrossRef]
28. Krauss, G. Austenite Grain-Size Control in Microalloyed Steel. In *Steels—Processing, Structure, and Performance, 2nd ed*; ASM International: Materials Park, OH, USA, 2015; pp. 153–157.
29. Pavlina, E.; Speer, J.; Van Tyne, C. Equilibrium Solubility Products of Molybdenum Carbide and Tungsten Carbide in Iron. *Scr. Mater.* **2012**, *66*, 243–246. [CrossRef]
30. Barraclough, D.; Whittaker, H.; Nair, K.; Sellars, C. Effect of Specimen Geometry on Hot Torsion Test Results for Solid and Tubular Specimens. *J. Test. Eval.* **1973**, *1*, 220–226.
31. Fechte-Heinen, R.; thyssenkrupp Steel Europe AG, Duisburg, Germany. Personal communication, 2018.
32. *ASTM Standard E384-17: Standard Test Method for Microindentation Hardness of Materials*; ASTM International: West Conshohocken, PA, USA, 2017.
33. Brito, R.; Kestenbach, H. On the Dispersion Hardening Potential of Interphase Precipitation in Micro-Alloyed Niobium Steel. *J. Mater. Sci.* **1981**, *16*, 1257–1263. [CrossRef]